Alignment and Calibration of Optical and Inertial Sensors Using Stellar Observations

Major M. Veth, *Air Force Institute of Technology*
J. Raquet, *Air Force Institute of Technology*

BIOGRAPHY

Major Mike Veth is a Ph.D. student in the Department of Electrical and Computer Engineering at the Air Force Institute of Technology. His current research focus is on the fusion of optical and inertial systems. He received his M.S. in Electrical Engineering from the Air Force Institute of Technology, and a B.S. in Electrical Engineering from Purdue University. In addition, Major Veth is a graduate of the Air Force Test Pilot School.

John Raquet is an associate professor in the Department of Electrical and Computer Engineering at the Air Force Institute of Technology, where he is responsible for teaching and research relating to GPS and inertial navigation systems. He received his Ph.D. in Geomatics Engineering from The University of Calgary, an M.S. in Aero/Astro Engineering from The Massachusetts Institute of Technology, and a B.S. in Astronautical Engineering from The U.S. Air Force Academy.

ABSTRACT

Aircraft navigation information (position, velocity, and attitude) can be determined using optical measurements from an imaging sensor pointed toward the ground combined with an inertial navigation system. A critical factor governing the level of accuracy achievable in such a system is the alignment and calibration of the sensors. Currently, alignment accuracy is limited by machining and mounting tolerances for low-cost applications.

In this paper, a novel alignment and calibration method is proposed which combines inertial and stellar observations using an extended Kalman filter algorithm. The approach is verified using simulation and experimental data, and conclusions regarding alignment accuracy versus sensor quality are drawn.

INTRODUCTION

Motivation

The development of low-cost inertial and optical sensors has led to remarkable advances in the field of optical-aided navigation (e.g., [14], [15]). In these systems, digital images are combined with inertial measurements to estimate position, velocity, and attitude. The relative orientation between the inertial and optical sensors is a critical quantity which must be determined prior to operation of the system. The accuracy with which the relative orientation is known effectively sets the lower bound for the navigation accuracy of the system.

In this paper, current alignment methods are discussed, and a novel method is presented which addresses the shortcomings of the current techniques. The algorithm is then tested using both simulated and flight data. Finally, conclusions are drawn regarding the fundamental limits of accuracy achievable given various system parameters and alignment procedures. This work is part of ongoing research into fusion of optical and inertial sensors for long-term autonomous navigation [12].

Current Methods

The ultimate goal of the alignment process is to determine the relative orientation between an optical and inertial sensor, or more specifically, the sensitive axes of both sensors. The methods used to estimate this orientation fall into two categories: mechanical and estimation-based techniques.

Mechanical techniques use mechanical measurements (such as laser theodolites) to determine the relative orientation between known fiducials on each sensor. This method requires knowledge of the relationship between the sensitive axes of the sensors and the external reference fiducials, which is subject to unknown manufacturing errors. In addition, depending on the required accuracy, this method requires external equipment which is not suitable for use in the field.

Report Documentation Page

Form Approved
OMB No. 0704-0188

1. REPORT DATE	2. REPORT TYPE	3. DATES COVERED
2007		**00-00-2007 to 00-00-2007**

4. TITLE AND SUBTITLE	5a. CONTRACT NUMBER
Alignment and Calibration of Optical and Inertial Sensors Using Stellar Observations	5b. GRANT NUMBER
	5c. PROGRAM ELEMENT NUMBER
6. AUTHOR(S)	5d. PROJECT NUMBER
	5e. TASK NUMBER
	5f. WORK UNIT NUMBER
7. PERFORMING ORGANIZATION NAME(S) AND ADDRESS(ES) **Air Force Institute of Technology,2950 Hobson Way,Wright Patterson AFB,OH,45433-7765**	8. PERFORMING ORGANIZATION REPORT NUMBER
9. SPONSORING/MONITORING AGENCY NAME(S) AND ADDRESS(ES)	10. SPONSOR/MONITOR'S ACRONYM(S)
	11. SPONSOR/MONITOR'S REPORT NUMBER(S)

12. DISTRIBUTION/AVAILABILITY STATEMENT
Approved for public release; distribution unlimited

13. SUPPLEMENTARY NOTES
The original document contains color images.

14. ABSTRACT

15. SUBJECT TERMS

16. SECURITY CLASSIFICATION OF:			17. LIMITATION OF ABSTRACT	18. NUMBER OF PAGES	19a. NAME OF RESPONSIBLE PERSON
a. REPORT	b. ABSTRACT	c. THIS PAGE			
unclassified	**unclassified**	**unclassified**		**10**	

Standard Form 298 (Rev. 8-98)
Prescribed by ANSI Std Z39-18

Estimation-based techniques utilize actual sensor measurements while subjecting the system to known conditions. In [8], the sensors are mounted on a calibrated pendulum while imaging a reference pattern. The orientation of the scene detected by the optical sensor, combined with the current local gravity vector, is used to estimate the relative orientation and inertial sensor biases.

These current approaches require dedicated equipment which would increase the difficulty of field calibrations. In addition, these "captive" techniques separate the calibration and navigation functions of the system and cannot compensate for time-varying errors due to temperature changes, flight profile, flexure modes, etc. In the next section, the basis for a real-time estimator which incorporates measurements of visual objects at known locations, inertial measurements, and position updates is developed. More specifically, the field of visible stars is used to provide the reference for the optical system.

The method proposed in this paper has several advantages over the current approaches. First, the system is automatic and requires no operator involvement or external equipment. Secondly, this method is not limited to stationary operation and can be accomplished during a mission. In fact, maneuvers can actually improve the observability of inertial sensor errors [13]. Finally, the recursive estimation approach allows the system to account for time-varying errors (e.g., accelerometer and gyroscope bias) in a more rigorous fashion than batch approaches.

There are some obvious disadvantages to using stellar observations which must be considered. Stellar observations require visibility of the sky or portions of the sky. In addition, the imaging system must be of appropriate sensitivity and measurement fidelity to resolve the location of celestial objects.

DEVELOPMENT

The method proposed in this paper employs an extended Kalman filter (EKF) algorithm (see [10], [11]) to recursively estimate camera alignment and calibration parameters by measuring the pixel locations of celestial objects in an image-aided inertial system.

Assumptions

This method is based on the following assumptions.

- A strapdown intertial measurement unit (IMU) is rigidly attached to a camera. Synchronized raw measurements are available from both sensors.
- The sensors are located at either a fixed, known location or external position measurements are available for a moving trajectory (e.g., Global Positioning System).
- A star tracking algorithm is available which can identify and track celestial objects.

Algorithm Description

In order to provide the maximum flexibility with respect to either fixed or moving trajectories, the estimator combines inertial measurements, optical measurements of known stars, and external position/velocity measurements. The system parameters (see Table 1) consist of the navigation parameters (position, velocity, and attitude), inertial measurement biases, and camera alignment and scale factor parameters. The navigation parameters are calculated using velocity increment ($\Delta\mathbf{v}^b$) and angular increment ($\Delta\boldsymbol{\theta}^b_{ib}$) measurements from the inertial navigation sensor which have been corrected for bias errors using the current bias estimates. These measurements are integrated from an initial state in the navigation (local-level) frame using mechanization algorithms described in [16].

Table 1: *System Parameter Definition*

Parameter	Description
$\mathbf{p}^n$	Vehicle position in navigation frame (latitude, longitude, altitude)
$\mathbf{v}^n$	Vehicle velocity in navigation frame (north, east, down)
$\mathbf{C}^n_b$	Vehicle body to navigation frame DCM
$\mathbf{a}^b$	Acclerometer bias vector
$\mathbf{b}^b$	Gyroscope bias vector
$\mathbf{C}^b_c$	Camera to vehicle body frame DCM
s_x	Camera image plane vertical scale factor
s_y	Camera image plane horizontal scale factor

An Extended Kalman Filter was constructed to estimate the errors in the calculated system parameters. In order to minimize the effects of linearization errors, the system parameters were periodically corrected by removing the current error estimate (see [10]). A block diagram of the system is shown in Figure 1.

The Kalman filter state vector, $\hat{\mathbf{x}}$, is defined as

$$\hat{\mathbf{x}} = \begin{bmatrix} \delta\hat{\mathbf{p}}^n \\ \delta\hat{\mathbf{v}}^n \\ \hat{\boldsymbol{\psi}} \\ \delta\hat{\mathbf{a}}^b \\ \delta\hat{\mathbf{b}}^b \\ \hat{\boldsymbol{\alpha}} \\ \delta\hat{s}_x \\ \delta\hat{s}_y \end{bmatrix} \tag{1}$$

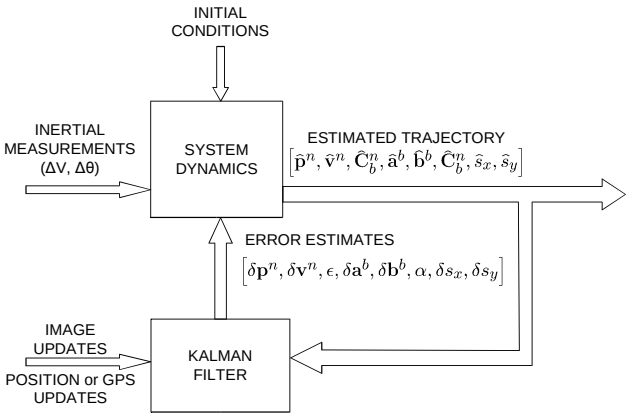

Figure 1: *Camera calibration extended Kalman filter block diagram. In this filter, surveyed position or GPS pseudo-range measurements and optical measurements of known stars are used to estimate trajectory errors from a reference trajectory provided by an inertial navigation system (INS). The errors are then "fed-back" and subtracted from the INS trajectory in order to keep the reference trajectory as close as possible to the true trajectory.*

where $\delta\hat{\mathbf{p}}^n$ is the estimated position error vector, $\delta\hat{\mathbf{v}}^n$ is the estimated velocity error vector, and $\hat{\boldsymbol{\psi}}$ is the estimated body-to-navigation frame attitude error (defined as small-angle rotations about the north, east, and down axes). The accelerometer and gyroscope bias errors are represented by $\delta\hat{\mathbf{a}}^b$ and $\delta\hat{\mathbf{b}}^b$, respectively. The camera alignment errors are represented by $\hat{\boldsymbol{\alpha}}$ (defined as small angle rotations about the camera x,y, and z axes) and scale factor by $\delta\hat{s}_x$,$\delta\hat{s}_y$ (defined later in Eqn. (5)).

The position, velocity, and attitude errors were modeled as a stochastic process based on the well-known Pinson navigation error model [16]. The accelerometer and gyroscopic bias errors were each modeled as a first-order Gauss-Markov process [10], based on the specification for the inertial measurement unit (IMU). The camera misalignment and scalefactor errors are modeled as unknown biases. A small amount of process noise is added to the state dynamics to promote filter stability [11].

Celestial Measurement Model

The celestial measurement is simply the current pixel location of an identified celestial object. Celestial object n is located at a known direction relative to the Earth (based on astronomical almanac data) [7], and is represented by the unit vector, $\hat{\mathbf{s}}_n^e(t_i)$, at time t_i [4]. The object direction vector in the camera frame, $\hat{\mathbf{s}}_n^c(t_i)$, is a function of the vehicle position, vehicle orientation, and camera-to-body orientation:

$$\hat{\mathbf{s}}_n^c(t_i) = \mathbf{C}_b^c\mathbf{C}_n^b\mathbf{C}_e^n\hat{\mathbf{s}}_n^e(t_i) \tag{2}$$

where $\mathbf{C}_e^n$ is the Earth frame to navigation frame direction cosine matrix. Using the pinhole camera model described in [9], the pixel location, $\mathbf{z}(t_i)$, is a function of the camera projection matrix, $\mathbf{\Pi}$,

$$\mathbf{z}(t_i) = \mathbf{\Pi}\underline{\mathbf{s}}_n^c(t_i) + \mathbf{v}(t_i) \tag{3}$$

where $\underline{\mathbf{s}}_n^c(t)$ is the homogeneous[1] form of the object direction vector in the camera frame. In this paper, an underbar indicates the homogeneous form of the vector (e.g., $\underline{\mathbf{s}}$ is the homogeneous form of $\mathbf{s}$). The measurement is corrupted by v, a zero-mean, white, Gaussian noise process with covariance

$$E\left[\mathbf{v}(t_i)\mathbf{v}^t(t_j)\right] = \begin{cases} \mathbf{R} & t_i = t_j \\ \mathbf{0} & t_i \neq t_j \end{cases} \tag{4}$$

The projection matrix is given by

$$\mathbf{\Pi} = \begin{bmatrix} s_x & 0 & b_x \\ 0 & s_y & b_y \end{bmatrix} \tag{5}$$

where s_x and s_y are camera scaling parameters in the x and y directions, respectively and b_x and b_y are the known x and y location of the image plane origin. Note that the image plane origin effectively defines the camera z axis, so the values of b_x and b_y are not modeled as states.

Thus the pixel measurement of a star's location is a nonlinear function of the true state corrupted by additive white Gaussian noise, and is represented by

$$\mathbf{z} = \mathbf{h}\left[\mathbf{p}^n, \mathbf{C}_b^n, \mathbf{C}_c^b, s_x, s_y\right] + \mathbf{v} \tag{6}$$

or, equivalently,

$$\mathbf{z} = \mathbf{h}\left[\mathbf{x}\right] + \mathbf{v} \tag{7}$$

The linearized observation matrix, $\mathbf{H}$, is the Jacobian of the nonlinear measurement function, $\mathbf{h}[\cdot]$, linearized about the reference trajectory, $\bar{\mathbf{x}}$:

$$\mathbf{H} = \left.\frac{\partial\mathbf{h}}{\partial\mathbf{x}}\right|_{\mathbf{x}=\bar{\mathbf{x}}} \tag{8}$$

The partial derivatives are calculated about the reference trajectory, starting with the camera scale factor states. Using Equation (3) as a reference, the partial derivatives are

$$\left[\frac{\partial\mathbf{h}}{\partial s_x}\frac{\partial\mathbf{h}}{\partial s_y}\right] = \begin{bmatrix}\mathbf{I}_{2\times2} & 0 \\ & 0\end{bmatrix}\underline{\mathbf{s}}_n^c \tag{9}$$

The partial derivative with respect to position is expressed by

$$\frac{\partial\mathbf{h}}{\partial\mathbf{p}^n} = \mathbf{\Pi}\frac{\partial\underline{\mathbf{s}}_n^c}{\partial\mathbf{p}^n} \tag{10}$$

[1]The homogeneous form of a vector is that vector augmented with a "1". The homogeneous form of the vector $\begin{bmatrix} x & y \end{bmatrix}^T$ is $\begin{bmatrix} x & y & 1 \end{bmatrix}^T$.

where,

$$\frac{\partial \underline{\mathbf{s}}_n^c}{\partial \mathbf{p}^n} = \frac{\frac{\partial \mathbf{s}_n^c}{\partial \mathbf{p}^n} - \underline{\mathbf{s}}_n^c \frac{\partial \mathbf{s}_n^c}{\partial \mathbf{p}^n}}{s_{n_z}^c} \tag{11}$$

and,

$$\frac{\partial \mathbf{s}_n^c}{\partial \mathbf{p}^n} = \mathbf{C}_b^c \mathbf{C}_n^b \left[\begin{array}{c|c|c} \mathbf{x}_1 & \mathbf{x}_2 & \mathbf{0}_{3\times 1} \end{array} \right]_{3\times 3} \tag{12}$$

where

$$\mathbf{x}_1 = \begin{pmatrix} 0 \\ 1 \\ 0 \end{pmatrix} \times (\mathbf{C}_e^n \mathbf{s}_n^e) \tag{13}$$

$$\mathbf{x}_2 = \mathbf{C}_e^n \left[\begin{pmatrix} 0 \\ 0 \\ -1 \end{pmatrix} \times \right] \mathbf{s}_n^e \tag{14}$$

The partial derivative with respect to body-to-navigation frame misalignment angle vector, $\boldsymbol{\psi}$, is

$$\frac{\partial \mathbf{h}}{\partial \boldsymbol{\psi}} = \mathbf{\Pi} \frac{\partial \underline{\mathbf{s}}_n^c}{\partial \boldsymbol{\psi}} \tag{15}$$

where

$$\frac{\partial \underline{\mathbf{s}}_n^c}{\partial \boldsymbol{\psi}} = \frac{\frac{\partial \mathbf{s}_n^c}{\partial \boldsymbol{\psi}} - \underline{\mathbf{s}}_n^c \frac{\partial \mathbf{s}_n^c}{\partial \boldsymbol{\psi}}}{s_{n_z}^c} \tag{16}$$

and

$$\frac{\partial \mathbf{s}_n^c}{\partial \boldsymbol{\psi}} = \mathbf{C}_b^c \mathbf{C}_n^b \left[(\mathbf{C}_e^n \mathbf{s}_n^e) \times \right] \tag{17}$$

The skew symmetric operator, $(\cdot)\times$, is defined as

$$\mathbf{s}_n^c \times = \begin{bmatrix} s_{n_x}^c \\ s_{n_y}^c \\ s_{n_z}^c \end{bmatrix} \times = \begin{bmatrix} 0 & -s_{n_z}^c & s_{n_y}^c \\ s_{n_z}^c & 0 & -s_{n_x}^c \\ -s_{n_y}^c & s_{n_x}^c & 0 \end{bmatrix} \tag{18}$$

Finally, the partial derivative with respect to the camera-to-body frame misalignment angle, $\boldsymbol{\alpha}$, is

$$\frac{\partial \mathbf{h}}{\partial \boldsymbol{\alpha}} = \mathbf{\Pi} \frac{\partial \underline{\mathbf{s}}_n^c}{\partial \boldsymbol{\alpha}} \tag{19}$$

where

$$\frac{\partial \underline{\mathbf{s}}_n^c}{\partial \boldsymbol{\alpha}} = \frac{\frac{\partial \mathbf{s}_n^c}{\partial \boldsymbol{\alpha}} - \underline{\mathbf{s}}_n^c \frac{\partial \mathbf{s}_n^c}{\partial \boldsymbol{\alpha}}}{s_{n_z}^c} \tag{20}$$

and

$$\frac{\partial \mathbf{s}_n^c}{\partial \boldsymbol{\alpha}} = \mathbf{C}_b^c \left[\left(\mathbf{C}_n^b \mathbf{C}_e^n \mathbf{s}_n^e \right) \times \right] \tag{21}$$

All other partial derivatives are zero.

The resulting observation matrix is

$$\mathbf{H} = \left[\begin{array}{ccccccc} \frac{\partial \mathbf{h}}{\partial \mathbf{p}^n} & \mathbf{0}_{3\times 3} & \frac{\partial \mathbf{h}}{\partial \boldsymbol{\psi}} & \mathbf{0}_{3\times 6} & \frac{\partial \mathbf{h}}{\partial \boldsymbol{\alpha}} & \frac{\partial \mathbf{h}}{\partial s_x} & \frac{\partial \mathbf{h}}{\partial s_y} \end{array} \right] \tag{22}$$

Updates

As mentioned previously, position measurements are also used to update the Kalman filter. For this research, surveyed position and zero velocity values are used to update the filter during stationary profiles. During flight profiles, single-channel pseudorange measurements from the Global Positioning System (GPS) are utilized. An example of a tightly coupled GPS measurement model is presented in [1].

RESULTS

The estimation algorithm was tested using both simulated profiles and a real profile flown on a T-38 aircraft. Simulations were constructed to determine the estimation accuracy, robustness, and sensitivity of the algorithm. The flight data were used to demonstrate observability of the camera calibration states during operational scenarios. In addition, the flight data helped to verify the accuracy of the astronomical almanac calculations.

Simulation

The simulations were based on a stationary profile designed to provide strong observability of the IMU biases and camera calibration parameters. This was achieved by periodically changing the orientation of the sensor in increments of 60 degrees while maintaining a view of the sky. The stationary profile is shown in Table 2.

Table 2: *Stationary camera calibration profile. The profile was designed to provide strong observability of IMU biases while maintaining a view of the sky.*

Segment	Roll (deg)	Pitch (deg)	Hdg (deg)
1	+60	0	0
2	-60	0	0
3	-60	0	60
4	+60	0	60
5	+60	0	120
6	-60	0	120

The simulations were conducted using three IMU models representing samples from consumer grade, tactical grade, and navigation grade sensors. The camera model was based on the gated-intensified CCD camera used during the Peeping Talon flight tests [12]. The camera produced 480 by 720 pixel interlaced images with a field of view of approximately 10 by 15 degrees. Image updates were processed at five-second intervals.

The IMU models represent typical performance of consumer-grade, tactical grade, and navigation grade sensors. The measurement parameters for each sensor are

Table 3: *Inertial measurement sensor specifications for the Cloud Cap Technology Crista consumer-grade IMU [2], Honeywell HG1700 tactical-grade IMU [5], and Honeywell HG9900 navigation-grade IMU [6]. The parameters noted with an asterisk were not included in the specifications and are estimates.*

Parameter (Units)	Crista IMU	HG1700	HG9900
Sampling interval (ms)	5.0	10.0	3.906
Gyro bias sigma (deg/hr)	1800	1.0	0.0015
Gyro bias time constant (hr)	2^*	2^*	2^*
Angular random walk ($deg/\sqrt{hr}$)	2.23	0.3	0.002
Gyro scalefactor sigma (PPM)	10000	150	5
Accel bias sigma (m/s^2)	0.196	0.0098	2.45×10^{-4}
Accel bias time constant (hr)	2^*	2^*	2^*
Velocity random walk ($m/s/\sqrt{hr}$)	0.261	0.57^*	0.0143^*
Accel scalefactor sigma (PPM)	10000	300	100

listed in Table 3.

Monte-carlo simulation results show that the algorithm accurately and robustly estimates both the camera to body alignment and camera scale factor parameters. Sample error functions are shown for the HG1700 IMU sensor, which are representative of the ensemble, in Figures 2, 3, 4, and 5. The rotations in the alignment profile clearly improve the observability of the camera alignment parameters as the filter errors (and uncertainty) decrease after each rotation maneuver. Note the alignment angles are essentially unobservable until the first rotation maneuver. The scale factor parameters' observability is largely independent of maneuvers, especially with a well-populated starfield. This would not be the case with a small number of available star measurements.

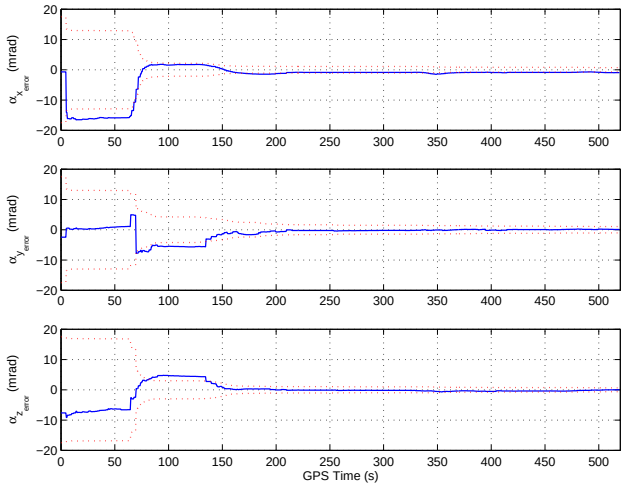

Figure 2: *Typical camera to body alignment estimation accuracy for the Crista IMU during the simulated alignment profile. The solid line represents the filter angular estimation errors and the dotted line represents the estimated standard deviation of the errors.*

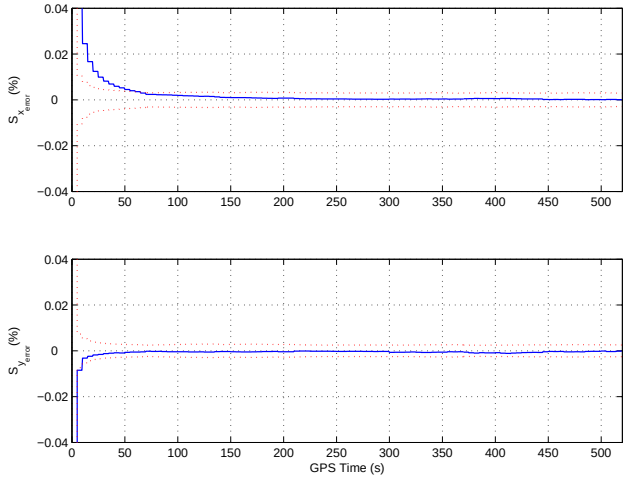

Figure 3: *Typical camera scale factor estimation accuracy for the Crista IMU during the simulated alignment profile. The solid line represents the filter angular estimation errors and the dotted line represents the estimated standard deviation of the errors.*

A qualitative estimate of achievable camera to body alignment accuracy for various inertial sensor models as a function of gyroscope random walk is shown in Figure 6. As expected, improving the quality of the inertial sensor yields improved alignment, up to the accuracy of the image sensor to resolve the star locations. In this case, the camera alignment estimate for the HG9900 is limited by the image measurements. This could be improved by increasing the angular sampling frequency of the imaging sensor [3]. A sensitivity analysis was performed by creating theoretical combinations of accelerometer and gyroscopic sensors and estimating the boresight alignment accuracy using the standard alignment profile. The results, shown in Table (4), indicate the performance of the gyroscope has a stronger contribution to the achievable boresight accuracy, although both sensors influence the ultimate performance due to cou-

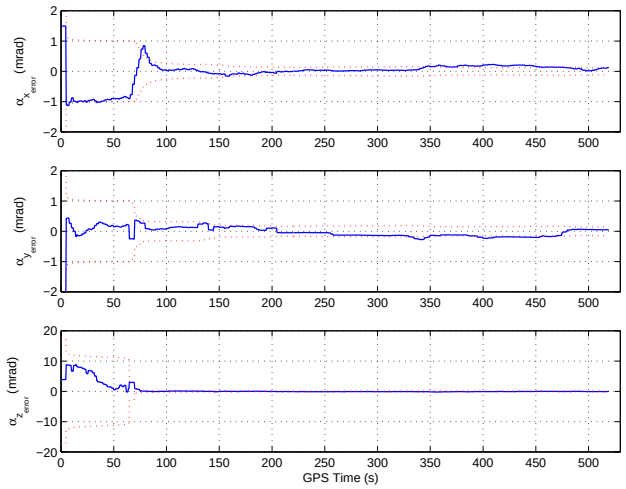

Figure 4: *Typical camera to body alignment estimation accuracy for the Honeywell H-1700 IMU during the simulated alignment profile. The solid line represents the filter angular estimation errors and the dotted line represents the estimated standard deviation of the errors.*

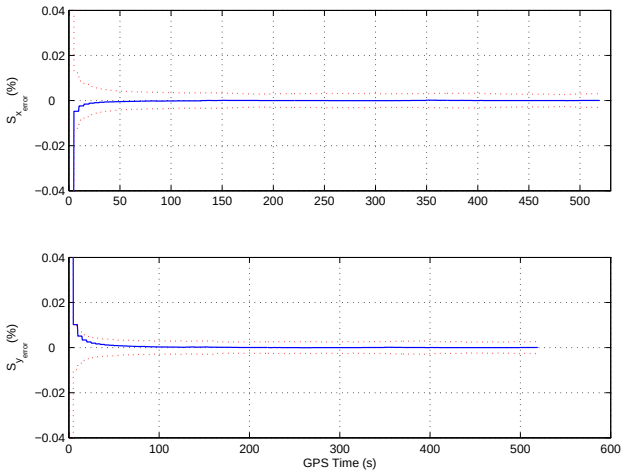

Figure 5: *Typical camera scale factor estimation accuracy for the Honeywell HG1700 IMU during the simulated alignment profile. The solid line represents the filter angular estimation errors and the dotted line represents the estimated standard deviation of the errors.*

pling between accelerometer and gyro error states.

These results illustrate the relationship between the accuracy of the optical and inertial sensors and the ability to determine the relative orientation of the sensors. More fundamentally, even if a mechanical or other method existed to provide a "better" alignment (e.g., relative to the "case"), it would be impossible to prove as the sensor measurements limit the observability of the relative alignment.

T-38 Flight Data Collection

In order to test the algorithm, a flight test was performed at Edwards Air Force Base as part of the joint AFIT/Test Pilot School (TPS) program. The test platform consisted of a T-38 aircraft, with the test configuration shown in Figure 7. The gated-intensified CCD camera was mounted inside the canopy, pointing out of the right side of the aircraft. The images were recorded using a Sony digital video recorder, and a GPS time tag (accurate to 1 ms) was generated by a time-code generator and time inserter, and recorded directly onto the video image. A liquid crystal display (LCD) monitor was provided for the pilot to see the camera images during the flight.

The inertial measurements were obtained from a Honeywell H-764G (HG9900 core) Embedded GPS/INS (EGI) navigation system modified to produce high rate (256 Hz) raw $\Delta\mathbf{v}^b$ and $\Delta\boldsymbol{\theta}_{ib}^b$ measurements. Finally, an Ashtech Z-surveyor semi-codeless receiver was used to collect dual-frequency GPS measurements. The L1-C/A code pseudorange measurements were used to provide a position update source to the Kalman filter during the profile. A second Z-surveyor was used as a differential reference station, and a carrier-smoothed code differential GPS trajectory was generated to serve as a precise truth trajectory.

The camera calibration estimation was conducted during a left turning profile, which provided an unobstructed view of the sky. A total of 92 images were used to update the Kalman filter during a 45 second period. The first image used as a measurement is shown in Figure 8. The filter's estimate of the stars locations along with covariance ellipses are overlayed on the image. This first image shows relatively large uncertainty ellipses, indicating a high level of uncertainty in the camera calibration. Figure 9 shows the second image measurement. After incorporating the first image measurement, the uncertainty ellipses have collapsed, which indicates the filter has increased confidence in the camera calibration. In addition, the tracked stars appear within their respective ellipses, which indicates the filter has estimated the camera calibration properly.

The estimated uncertainty of the camera alignment and scale factor states are shown in Figures 10 and 11, respectively. Note the filter achieves a nearly steady-state level of confidence after approximately 15 seconds of image updates.

Table 4: *Camera to inertial alignment accuracy accelerometer / gyroscope performance sensitivity. Theoretical alignment performance (in $1-\sigma$ RMS arcseconds) is shown as a function of various combinations of sensors from the Crista, HG1700, and HG9900 IMUs after completing the standard alignment profile.*

	HG9900 Gyro	HG1700 Gyro	Crista Gyro
HG9900 Accel	11.1”	22.7”	41.3”
HG1700 Accel	11.6”	45.4”	71.8”
Crista Accel	12.2”	68.1”	291.2”

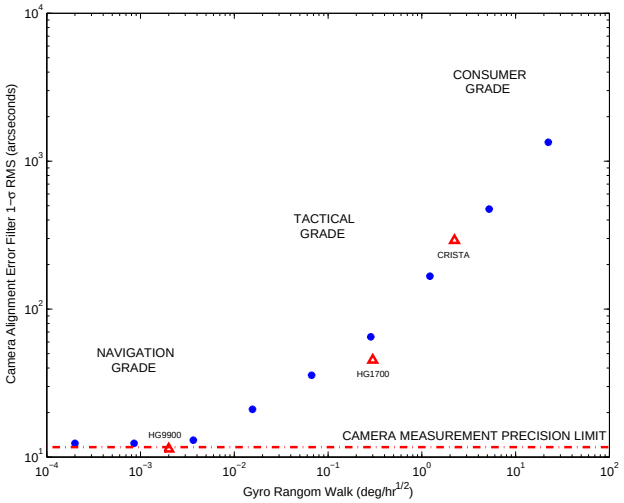

Figure 6: *Typical camera to inertial alignment accuracy for various grades of IMU. Specific results are shown for the Crista, HG1700, and HG9900 IMUs after completing*

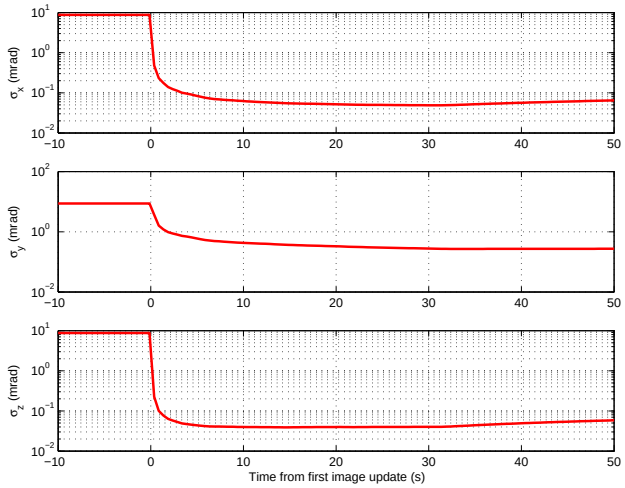

Figure 10: *Estimated uncertainty of camera to body alignment during T-38 flight profile. Celestial image updates were available for approximately 38 seconds.*

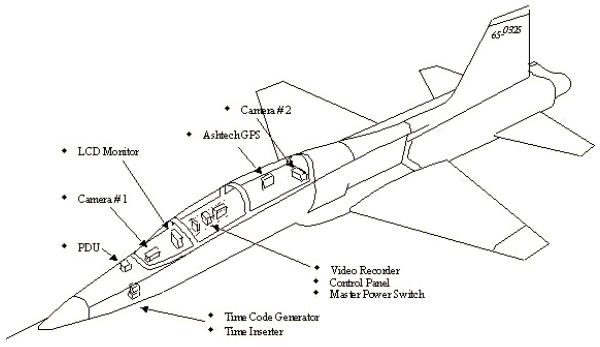

Figure 7: *Northrop T-38 instrumented with synchronized digital video camera and inertial navigation system.*

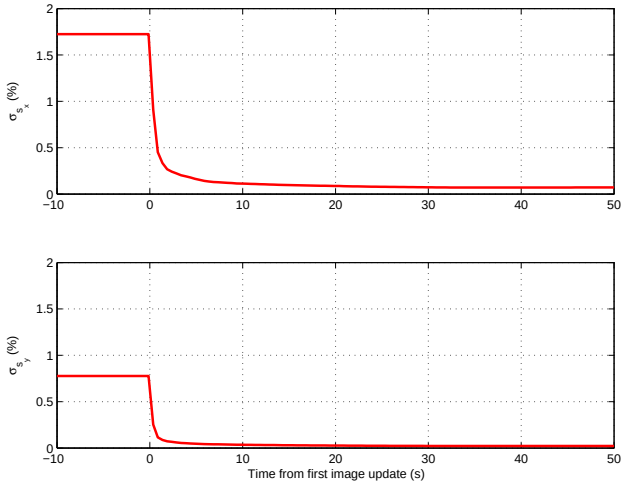

Figure 11: *Estimated uncertainty of camera scale factor parameters during T-38 flight profile. Celestial image updates were available for approximately 38 seconds.*

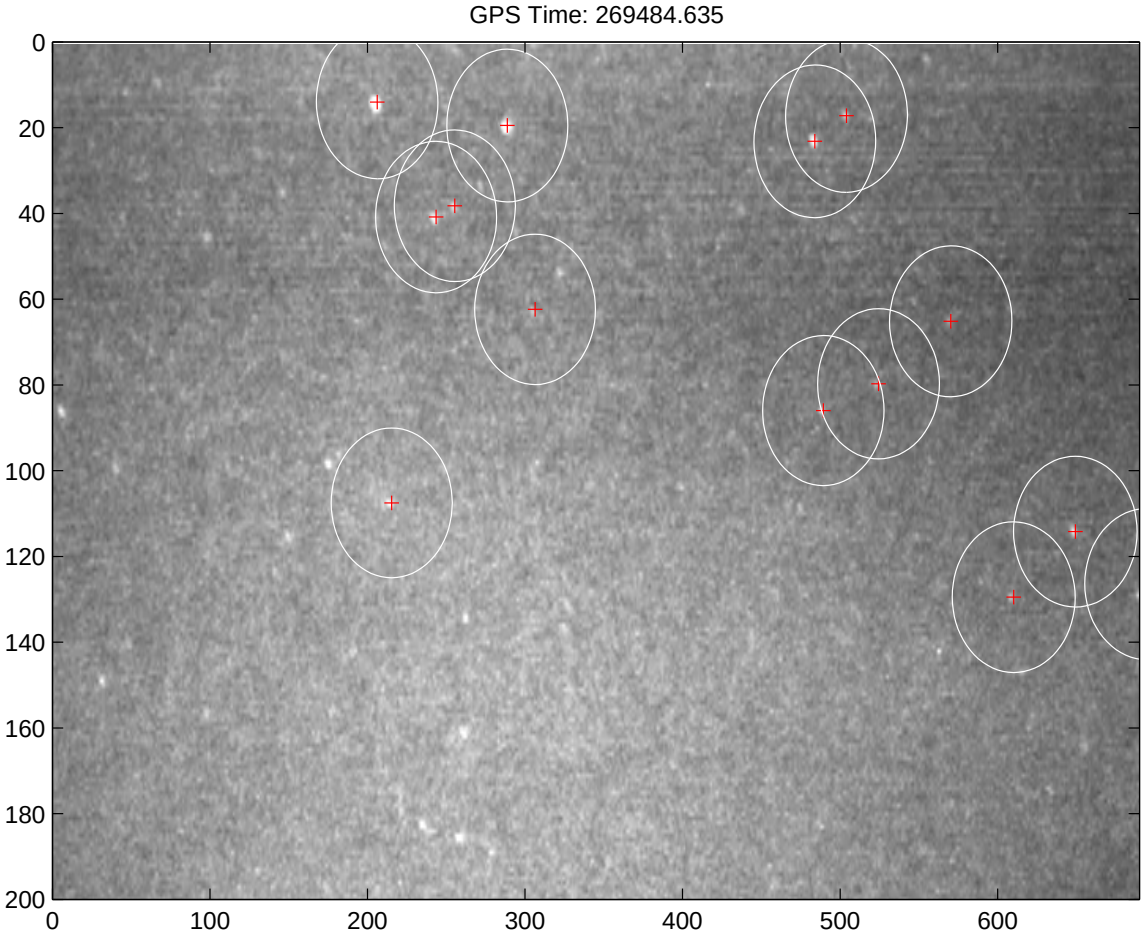

Figure 8: *Initial celestial update from Peeping Talon data collection. The position of the tracked stars is shown by a plus (+) symbol. The ellipses represent the Kalman filter's uncertainty of the true pixel location of each star.*

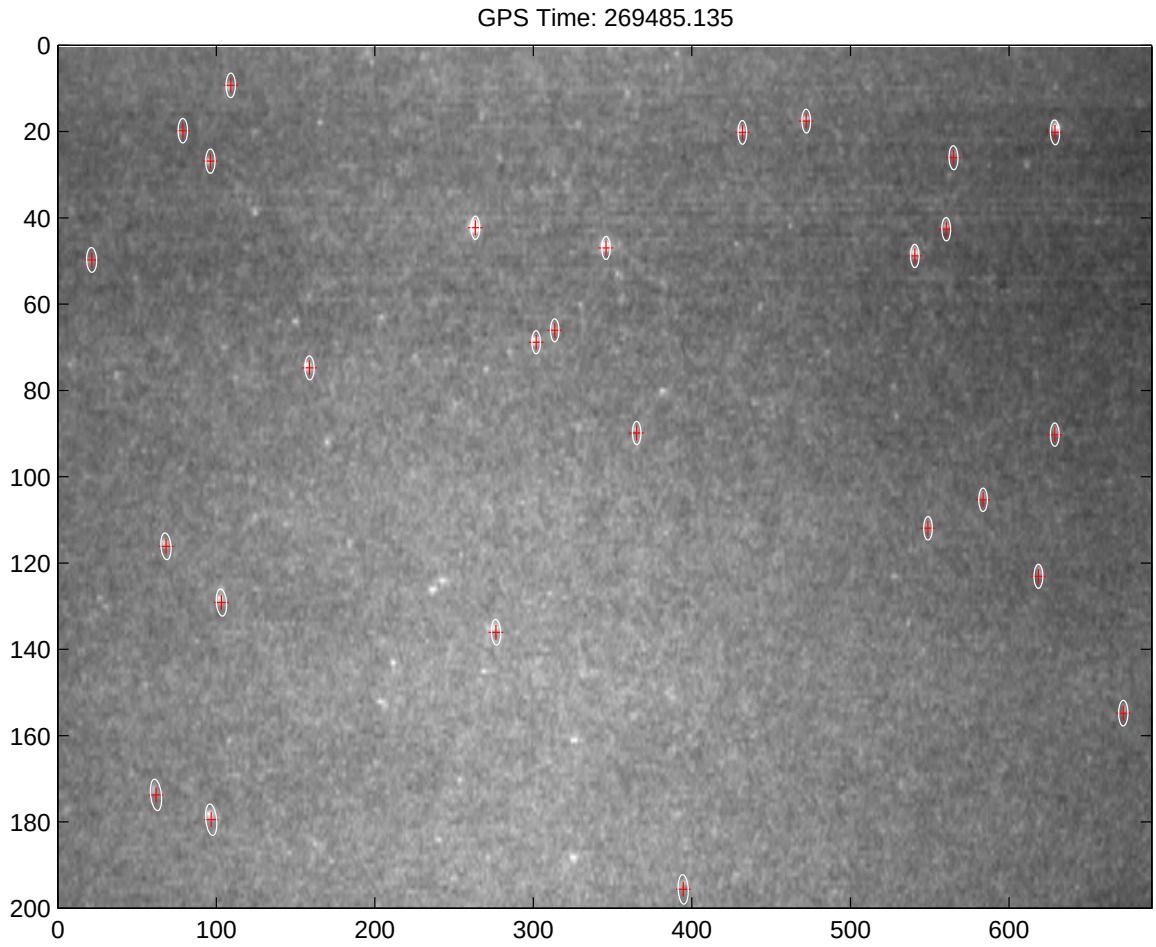

Figure 9: *Second celestial update from Peeping Talon data collection. The position of the tracked stars is shown by a plus (+) symbol. The ellipses represent the Kalman filter's uncertainty of the true pixel location of each star.*

CONCLUSIONS

In this paper, an algorithm is presented to estimate the camera calibration parameters of an optical-inertial system utilizing stellar observations and inertial measurements *in situ*. The algorithm is robust and suitable for various quality inertial sensors and trajectories, provided a position reference is available. As expected, the alignment quality achievable is a function of the accuracy of the inertial measurement unit and imaging sensor. In addition, profiles with angular changes are shown to improve system observability through simulation.

DISCLAIMER

The views expressed in this article are those of the author and do not reflect the official policy or position of the United States Air Force, Department of Defense, or the U.S Government.

References

[1] R. G. Brown and P. Y. Hwang. *Introduction to Random Signals and Applied Kalman Filtering*. John Wiley and Sons, Inc., New York, NY, 1992.

[2] Cloud Cap Technology. Crista Inertial Measurement Unit (IMU) Interface / Operation Document. Specification, May 2004. URL: http://www.coudcaptech.com/.

[3] J. W. Goodman. *Introduction to Fourier Optics*. McGraw Hill, Boston, Massachusetts, 1996.

[4] R. M. Green. *Spherical Astronomy*. Cambridge University Press, New York, NY, 1985.

[5] Honeywell International Inc. HG1700 Inertial Measurement Unit. Datasheet, August 2003.

[6] Honeywell International Inc. HG9900 Inertial Measurement Unit. Datasheet, 2004.

[7] G. Kaplan, J. Hughes, P. Siedelmann, C. Smith, and B. Yallop. Mean and Apparent Place Computations in the New IAU System. III. Apparent, Topocentric, and Astrometric Places of Planets and Stars. *The Astronomical Journal*, 97:1197–1210, April 1989.

[8] J. Lobo and J. Dias. Visual and Inertial Sensor Cooperation Using Gravity as a Vertical Reference. *IEEE Transactions on Pattern Analysis and Machine Intelligence*, 25:1597–1608, December 2003.

[9] Y. Ma, S. Soatto, J. Kosecka, and S. S. Sastry. *An Invitation to 3-D Vision*. Springer-Verlag New York, Inc., New York, New York, 2004.

[10] P. S. Maybeck. *Stochastic Models Estimation and Control, Vol I*. Academic Press, Inc., Orlando, Florida 32887, 1979.

[11] P. S. Maybeck. *Stochastic Models Estimation and Control, Vol II*. Academic Press, Inc., Orlando, Florida 32887, 1979.

[12] J. F. Raquet and M. Giebner. Navigation Using Optical Measurements of Objects at Unknown Locations. In *Proceedings of the 59th Annual Meeting of the Institute of Navigation*, pp. 282–290, June 2003.

[13] E.-H. Shin. Accuracy Improvement of Low Cost INS/GPS for Land Applications. Technical Report 20156, University of Calgary, Calgary, Canada, 2001.

[14] D. Strelow and S. Singh. Optimal Motion Estimation from Visual and Inertial Measurements. In *Proceedings of the Workshop on Applications of Computer Vision*, December 2002.

[15] D. Strelow and S. Singh. Online Motion Estimation from Visual and Inertial Measurements. In *Proceedings of the Workshop on Integration of Vision and Inertial Sensors (INERVIS 2003)*, June 2003.

[16] D. Titterton and J. Weston. *Strapdown Inertial Navigation Technology*. Peter Peregrinus Ltd., Lavenham, United Kingdom, 1997.